ACS Catalysis

pubs.acs.org/acscatalysis
Research Article

Structural Changes of Ni and Ni−Pt Methane Steam Reforming Catalysts During Activation, Reaction, and Deactivation Under Dynamic Reaction Conditions

Enrico Tusini, Maria Casapu, Anna Zimina, Dmitry E. Doronkin, Heike Störmer, Laurent Barthe, Stephanie Belin, and Jan-Dierk Grunwaldt*

Cite This: ACS Catal. 2024, 14, 7463−7477
Read Online

ACCESS | Metrics & More | Article Recommendations | Supporting Information

ABSTRACT: Ni-based catalysts are the most widely used materials to produce H_2 in large-scale methane steam reformers under stationary conditions. For domestic applications such as fuel cells, H_2 production involves the exposure of the catalysts to more dynamic conditions due to the daily startup and shutdown operation mode, making Ni-based catalysts susceptible to oxidation and deactivation. In this context, we report a systematic investigation of the structural changes occurring for monometallic Ni/$MgAlO_x$ and bimetallic NiPt/$MgAlO_x$ catalysts during methane steam reforming under transient conditions, comprising catalyst activation, operation, and deactivation processes. Besides extensive catalytic tests, the samples prepared by incipient wetness impregnation were characterized by complementary methods, including N_2-physisorption, X-ray diffraction, H_2-temperature-programmed reduction, and electron microscopy. Next, the structure of the Ni and Pt species was monitored under reaction conditions using time and spatially resolved *in situ*/*operando* X-ray absorption spectroscopy. The results obtained show that before catalyst activation by H_2-reduction, nickel diffuses into the support lattice and forms mixed oxides with magnesium. In the activated catalysts, Ni is present in the metallic state or alloyed with Pt. A clear beneficial effect of the noble metal addition was identified on both the activity and stability of the bimetallic NiPt/$MgAlO_x$ catalyst. In contrast, the pronounced oxidation and reincorporation of Ni into the support lattice were observed for the monometallic sample, and these catalyst deactivation effects are hindered in the bimetallic Ni−Pt catalyst. Overall, the outcome of our study not only helps in understanding the catalyst activation/deactivation processes at an atomic level but also provides the basis for the rational development of improved methane steam reforming catalysts.

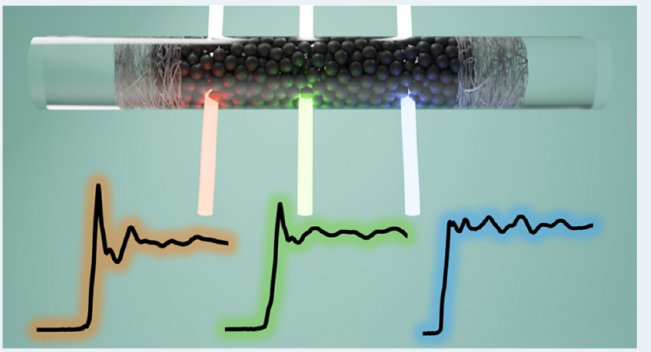

KEYWORDS: *operando characterization, X-ray absorption spectroscopy, methane steam reforming, bimetallic catalysts, hydrogen, transient conditions*

1. INTRODUCTION

The increase in population and the standard of living in the last decades caused an expansion in energy demand and consumption. Consequently, the exploitation of natural resources such as coal, oil, and gas increased, raising the emission of greenhouse gases (GHG) into the atmosphere to alarming levels. Hydrogen, which is an important raw material widely used in the chemical industry,[1,2] is now regarded as a possible solution to replace nonrenewable fossil fuels for a sustainable future. Based on the production methods, hydrogen sources can be divided into three main categories:[3] (i) gray hydrogen: fossil fuels derivative, involving CO_2 released into the atmosphere; (ii) blue hydrogen: fossil fuel-based production, with carbon capture, utilization, and storage (CCUS)-implemented systems, and (iii) green hydrogen: based on renewable resources. In spite of the great efforts and technical improvements done for a green hydrogen transition in the last decades, methane steam reforming (MSR) still holds for the vast majority of hydrogen production[4] to these days. Among numerous applications, hydrogen usage gained additional attention recently in polymer electrolyte fuel cells (PEFC), which could be applied for stationary-distributed power stations in buildings, residences in urban areas, or remote regions. These distributed smart grids have several advantages, including the ability to provide both heat and

Received: November 30, 2023
Revised: February 14, 2024
Accepted: March 19, 2024

electricity in a flexible way, thus leveling off the peaks in the power demand. Nonetheless, the lack of a robust hydrogen delivery infrastructure makes the technology not appealing to the final customer. A possible solution would be to use a fuel reformer, which is able to convert hydrogen-rich fuels into molecular hydrogen when required, by using fuels such as liquefied petroleum gas (LPG) and methane. Preferentially, the reforming reaction used is methane steam reforming since among the other possibilities—partial oxidation, autothermal reforming, and dry reforming— it is the most mature technology and yields the highest hydrogen concentration.[5,6] However, in contrast to the industrial-scale reformer, which operates under stationary conditions, systems for domestic purposes such as small-scale fuel reformers must withstand the transient conditions of numerous activity cycles. The bottleneck is, thus, to find a catalyst that can tolerate such rapid and rough changes in temperature and reaction mixture.

Ni-based catalysts supported on metal oxides (Al_2O_3, MgO, and their mixed oxides) have been intensively studied and industrially used for MSR.[7−9] The high catalytic activity and relatively low cost made them the perfect compromise for the industrial application of MSR. Nevertheless, Ni-based catalysts suffer from severe deactivation mechanisms, such as coke deposition, Ni oxidation, and sintering.[8,10,11] According to Matsumara and Nakamori's[12] X-ray diffraction (XRD) measurements of the catalysts supported on SiO_2 and Al_2O_3, prereduced Ni particles are progressively oxidized by steam under steady-state reaction conditions at 500°C. In contrast, on TiO_2 at the same reaction temperature Ni particles were reported to remain in the metallic state over 100 h testing time.[13] With respect to coke formation, low temperatures are known to promote carbon deposition if the H_2O/CH_4 ratio is close to stoichiometric.[14] To overcome these challenges, various synthesis methods have been applied for preparing Ni-catalysts on different supports and additional promoters were added for tuning the properties of the carrier or Ni particles.[9] The catalyst support is known to play a major role in affecting not only the state of Ni but directly contributing to the reaction mechanism, e.g., adsorption of reactants or as an oxygen storage component during coke removal.[15,16] The interactions of Ni with the Al- or Mg-based supports have been intensively studied in the literature. Generally, a weak interaction results in better reducibility of the active metal but poor stabilization against sintering; a strong interaction hinders the reduction of the active metal phase but allows the stabilization of small nanoparticles. Crucial factors for the modulation of metal−support interactions are the synthesis procedure and the calcination temperature.[17−19] Several studies[20−22] reported the formation of $NiAl_2O_4$ spinel phase after the thermal treatment of Ni supported on Al_2O_3, which then requires temperatures above 750 °C to be reactivated. Due to their similar atomic radius, the intercalation of Ni into Mg-based supports is also possible at any concentration.[23,24] In both cases, small nickel nanoparticles are formed upon reduction, which further prevents deactivation like carbon deposition and sintering.[25] With respect to the catalyst promoters, the doping of Ni particles with a secondary metal seems to be an effective solution against deactivation. Particularly, platinum-group metals (PGM) decorate or form alloys with Ni, often leading to improved activity and stability.[26−28]

These aspects have been extensively investigated during the past years but mostly by pre- and post-mortem analysis of catalysts. Despite monitoring the evolution of the catalyst during methane steam reforming (*in situ*/*operando*) would be highly valuable for a more comprehensive understanding of these systems, only a small number of such studies have been reported.[29,30] This is probably due to the harsh reaction conditions of the MSR process. By *operando* Fourier-transform infrared spectroscopy measurements on a series of Ni/SiO_2 catalysts, important reaction intermediates and rate-determining steps were identified for steam reforming and dry reforming of methane.[31] In a study by Duarte et al.,[32] the cerium oxidation state in CeO_2-doped Rh/Al_2O_3 catalysts was determined by *in situ* X-ray absorption spectroscopy (XAS) measurements during methane steam reforming at 500 °C, which allowed to relate its contribution to water activation and alumina stabilization by $CeAlO_3$ formation. By using the same approach, the effect of CeO_2 and Sm_2O_3 dopants on the Rh state and sintering behavior was also demonstrated in a subsequent study.[33] Particularly, hard X-ray-based techniques appear very promising due to the possibility of simultaneously obtaining information about the electronic state and the local structure surrounding the adsorbing atom under realistic reaction conditions. For such *in situ*/*operando* studies, different cells have been constructed over the past years to mimic realistic reaction conditions.[34,35] Concerning the steam reforming of methane, this reaction requires high temperatures (up to 900 °C) even during catalyst activation, and only a few *in situ*/*operando* setups exist, which are capable of fulfilling these conditions.[36−38] For instance, La Fontaine et al.[39] recently reported a reaction environment able to reach 1000 °C with various heating/cooling ramp rates, which is suitable also for methane steam reforming studies. Analogous, Eggart et al.[38] conducted *in situ*/*operando* XAS investigations up to 1000 °C with a newly developed cell.

In this context, the present work focuses on elucidating the structure of the active species in 15%Ni/$MgAlO_x$ and 15%Ni-1%Pt/$MgAlO_x$ catalysts under transient reaction conditions between room temperature and 900 °C, which are characteristic for small-scale fuel reformers with daily startup and shutdown (DSS) operation. Complementary *in situ*/*operando* X-ray absorption spectroscopy (XAS) and X-ray diffraction (XRD) measurements are used to reveal structural changes of Pt and Ni species together with support phase variations during catalyst activation and light-off/light-out cycles over a broad temperature range. Time and spatially resolved XAS measurements were conducted at Ni K and Pt L_3 edges under transient methane steam reforming reaction conditions to understand the activation/deactivation behavior of such monometallic and bimetallic catalysts.

2. EXPERIMENTAL METHODS

2.1. Catalyst Preparation. Commercially available hydrotalcite from SASOL GmbH (PURAL MG70) with Al_2O_3/MgO = 30:70 was used as support for both mono- and bimetallic Ni−Pt catalysts after calcination at 900° for 12 h in static air. The resulting material is referred to as $MgAlO_x$ in the following discussion. In the next step, the incipient wetness impregnation method (IWI) was used to add aqueous solutions of tetraamine platinum nitrate ($Pt(NH_3)_4(NO_3)_2$) and nickel nitrate hexahydrate ($Ni(NO_3)_2{\cdot}6H_2O$) precursors. The bimetallic Ni−Pt catalyst was prepared via coimpregnation. The metal concentrations selected for the mono- and bimetallic catalysts are, respectively, 15 wt % Ni and 1 wt % Pt. The resulting samples were dried at 80° for 12 h and

https://doi.org/10.1021/acscatal.3c05847
ACS Catal. 2024, 14, 7463−7477

subsequently calcined at 500° for 6 h in static air. In the following discussion, the mono- and bimetallic samples are denoted as Ni/$MgAlO_x$ and NiPt/$MgAlO_x$, respectively.

2.2. Catalyst Characterization. The Brunauer−Emmett−Teller (BET) surface area[40] of the samples was determined by N_2 physisorption at −196 °C using a BELSOPRP-mini instrument (MicrotracBEL, Osaka, Japan). Prior to the analysis, the samples were degassed at 200 °C for 2 h.

The crystallinity of the catalyst components was assessed via XRD using an X'Pert PRO instrument (PANalytical, Malvern, United Kingdom). The patterns were recorded between 5 and 120° using Cu Kα radiation (wavelength = 1.54 Å) with a step size of 0.017°.

Temperature-programmed reduction with H_2 (H_2-TPR) was performed on an AutoChem II instrument (Micromeritics, Norcross, USA) by heating the sample at 10 °C/min from room temperature to 900 °C while dosing 50 mL/min of 10% H_2/Ar. Before the reduction step, adsorbed species were removed by heating the sample in 50 mL/min of He from room temperature to 200 °C.

For all catalyst samples, Ni and Pt metal loadings were determined by inductively coupled plasma optical emission spectroscopy (ICP-OES) using an OPTIMA 4300 DV spectrometer (PerkinElmer, Waltham, USA).

2.3. *Operando* X-ray Absorption Spectroscopy Study. The *operando* XAS measurements were performed at the ROCK beamline[39,41] of SOLEIL Synchrotron (Saint-Aubin, France). For these experiments, the quick-EXAFS[42,43] (QEXAFS) acquisition mode was used with a time resolution of 2 Hz. Energies were selected via two independent crystal channel-cut monochromators (Si(111), Si(220)). The "edge jump" operation mode of the ROCK beamline[39,41] was used to monitor simultaneously the Ni K (8333 eV) and Pt L_3 (11564 eV) edges (the edge switch required ca. 1 min). During transient reaction conditions, the middle of the catalyst bed was monitored with a beam size of about 450 μm × 350 μm (H × V). For selected temperatures, three positions along the catalyst bed were screened (beginning, middle, and end of a catalyst bed of 6 mm, with about 2.5 mm in between the measured positions), in order to identify gradients in the oxidation state and structure for Ni and Pt during the reaction. For energy calibration, reference metal foils of Ni and Pt were recorded together with each experimental spectrum. For initial data collection and merging, a graphical user interface (GUI) developed at SOLEIL was used.[39,41] Further data evaluation was performed using Athena and Artemis data analysis software using IFEFFIT.[44] The extended X-ray absorption fine structure (EXAFS) data $\chi(k)$ collected at room temperature were extracted, background subtracted, and subsequently analyzed in the k-space range of 3−12 $Å^{-1}$ for both edges. For the Ni K edge, the Fourier-filtered R-space selected for the fitting is 1.0−3.1 Å, while for the Pt L_3 edge, the R-space selected is 1.0−2.5 Å. The passive electron reduction factor (S_0^2) estimated from the foil fitting is 0.78 for Pt and 0.83 for Ni. Complex systems such as catalytic materials require a mixture of various scattering paths to obtain a meaningful structure refinement. In this study, the Ni metal structure was used to model the Ni−Ni shell (ICSD collection code 260169), and $NiMgO_x$ was used for the Ni−Mg second scattering shell (ICSD collection code 13774). The Ni−O and Ni−Ni (second scattering shell) scattering paths are modeled starting from NiO (ICSD collection code 184918), while the Ni−Pt interaction (obtained via Pt L_3 edge data fitting) is modeled using a NiPt alloy structure (ICSD collection code 105318). Coordination numbers (CN), mean square deviation of interatomic distances (σ^2), interatomic distances (R), and energy shift (δE_0) are refined during the fitting. The overall misfit from data and fitting is expressed via the R factor.

For the *operando* experiments, 5 mg of catalyst (1:1 dilution with $MgAlO_x$ support, sieve fraction 100−200 μm) was loaded into a quartz capillary of 1.5 mm diameter (wall thickness of 0.02 mm). An *operando* XAS cell recently developed at the ROCK beamline was used for all experiments.[39] The cell can be used in both fluorescence and transmission data acquisition modes. Additionally, linear and uniform heating and cooling are provided between room temperature and 1000 °C, which was highly important for studying the catalysts during the methane steam reforming reaction. In the first step, the catalysts underwent a prereduction treatment (5% H_2/He, 50 mL/min total flow) while continuously monitoring Ni and Pt structure via continuously collecting QEXAFS spectra. Before and after each change in the reaction environment, a series of EXAFS spectra were recorded as well. Afterward, the reaction mixture (5000 ppm of CH_4, 1.5% H_2O in He; 50 mL/min total flow) was supplied to the catalyst using mass flow controllers (Bronkhorst) and a water vapors gas saturator (at RT) at a WHSV of 10^6 mL $g_{catalyst}^{-1}$ h^{-1} (comparable to the lab scale experiments). This gas mixture with a steam-to-carbon (S/C) ratio of 3 was selected to prevent the capillary reactor obstruction by carbon deposit formation, which is known to occur for S/C < 2.[45,46] Reaction products were monitored with a quadrupole mass spectrometer (Pfeiffer Vacuum, Omnistar GSD 320) and an online FTIR gas analyzer (MKS, Multigas 2030). Changes in the chemical state of the catalysts were monitored in the middle of the catalyst bed under transient reaction conditions (light-off/light-out cycles) by QEXAFS measurements at Ni K and Pt L_3 edges. Additionally, 3 different positions in the catalyst bed (beginning, middle, and end) were investigated at various temperatures during cooling down from 900 °C to room temperature after 3 consecutive activity light-offs.

2.4. *Operando* X-ray Powder Diffraction Study. *Operando* X-ray diffraction experiments were conducted at the DiffAbs beamline of SOLEIL Synchrotron (Saint-Aubin, France) during transient reaction conditions similar to those applied for the *operando* XAS measurements: (i) prereduction in 5%H_2/He; (ii) light-off/light-out cycles in the reaction mixture (5000 ppm of CH_4, 1.5% H_2O in He; 50 mL/min total flow). The energy selected was 8.3 keV, which was tuned using a double Si(111) crystal (3−23 keV) and two Rh-coated mirrors. A Circular Hybrid Pixel Array Detector[47] (CirPad) was used, which consists of 20 XPAD modules assembled together in a circular arch geometry, capable of covering angles up to 135° and an angular opening of 0.0115°. Due to the geometry of the CirPad, a gas blower (FMB Oxford, UK) was used to heat the capillary reactor. Light-off (L_{Off}) and light-out (L_{Out}) experiments were conducted in a similar manner as during the *operando* XAS experiments.

2.5. Catalytic Tests. Systematic catalytic tests were performed for all mono- and bimetallic catalysts in a plug flow reactor, similar to the one used for the *operando* XAS and XRD experiments. Because of the high temperature required for the reaction, a specially designed high-temperature oven was used.[38] Briefly, about 5 mg of sieved catalyst powder was pretreated in a 5%H_2/N_2 gas flow for 1 h at 900 °C. Afterward,

https://doi.org/10.1021/acscatal.3c05847
ACS Catal. 2024, 14, 7463−7477

the reaction was conducted in 5000 ppm of CH_4 and 1.5% H_2O, balanced to 50 mL/min in N_2 (roughly 10^6 mL/h/g_{cat}).

3. RESULTS AND DISCUSSION

3.1. Catalyst Characterization. Despite the high specific surface area of the as-received MG70 support (233 m^2/g), a pronounced drop was measured after calcination at 700 °C for 5 h (88 m^2/g). After Ni and Pt deposition, the BET surface area did not change significantly, amounting to 72 m^2/g for 15 wt % Ni/$MgAlO_x$, 86 m^2/g for 1 wt % Pt/$MgAlO_x$, and 72 m^2/g for 15% Ni-1% Pt/$MgAlO_x$ catalysts. Figure 1 shows the

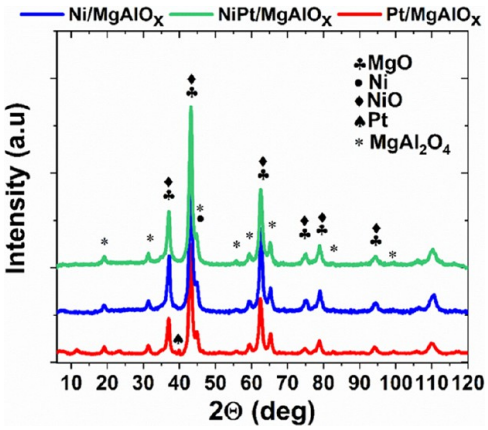

Figure 1. XRD patterns of the as-prepared mono- and bimetallic 15% Ni-1% Pt/$MgAlO_x$ catalysts.

corresponding X-ray diffractograms of the $MgAlO_x$ support as well as of the monometallic and bimetallic Pt−Ni catalyst samples. In the monometallic Ni/$MgAlO_x$ sample, diffraction peaks corresponding to $MgAl_2O_4$, MgO, and NiO phases can be observed. The simultaneous presence of MgO and $MgAl_2O_4$ is due to the nonstoichiometry of the starting hydrotalcite support. The identification of the individual NiO and MgO contributions is difficult due to the similarities of the unit cells. The same applies to $MgAl_2O_4$ and the possibly formed $NiAl_2O_4$ phases. However, a shift toward higher 2θ is noticed for the Ni/$MgAlO_x$ catalyst compared to the pure support,[48,49] which is probably caused by the intercalation of Ni^{2+} into the MgO lattice. Due to the relatively low loading, Pt addition does not seem to affect the catalyst's crystalline structure. Nonetheless, the absence of characteristic patterns for metallic Pt, as observed for the monometallic Pt/$MgAlO_x$ sample, indicates a possible interaction with Ni species, leading to a higher noble metal dispersion in the bimetallic catalyst.

The reduction behavior of Ni species in the Ni/$MgAlO_x$ and NiPt/$MgAlO_x$ catalysts was first investigated by means of H_2-TPR. The profiles of the thermal conductivity detector signals (Figure 2) recorded for the different samples show clear differences depending on the catalyst composition. For Ni-containing samples, two separate reduction regions are recognized: (i) a low-temperature region from 200 to 500 °C and (ii) a high-temperature region from 500 to 900 °C. The low-temperature region presents peaks around 409 and 339 °C, respectively, for Ni/$MgAlO_x$ and NiPt/$MgAlO_x$. At this temperature, the hydrogen consumption is mainly attributed to the presence of NiO particles on the catalyst surface, not in close contact with the support.[50] Between 600 and 750 °C, the reacting species are reported to be Ni^{2+} ions in the outermost layer and subsurface of mixed oxide phases.[48,51]

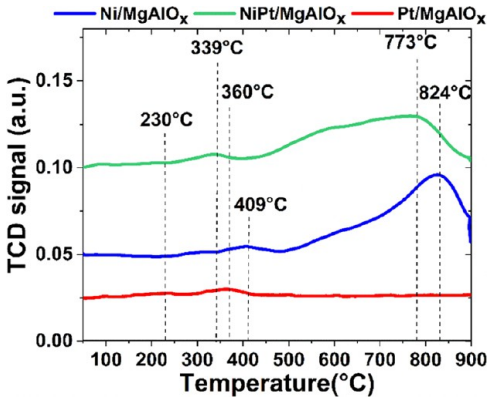

Figure 2. H_2-TPR profiles measured by a thermal conductivity detector (TCD) for the mono- and bimetallic samples using 10% H_2/Ar (50 mL/min, 100 mg sample, 10 °C/min heating rate).

At even higher temperatures, reduction peaks are mostly ascribed to the formation of the hardly reducible NiO−MgO solid solution,[50,3,52] sometimes also referred to as $Ni_xMg_yO_z$ or $NiMgO_x$, with a variable composition depending on the sample calcination temperature and the quantity of Ni present in the material. However, even though MgO represents the vast majority of the carrier material, the high reduction temperature was attributed in the literature to the possibly formed $NiAl_2O_4$.[53,54] The reduction of both phases, Ni_xMg_yO and $NiAl_2O_4$, as well as of other Ni species cannot be clearly elucidated by an H_2-TPR experiment but require a more detailed analysis as shown in the following discussion. Interestingly, Pt addition promotes the reduction of all Ni species, which is most probably caused by the hydrogen spillover effect after its dissociation on Pt.[55] Furthermore, the presence of platinum has been linked to an increase in the dispersion of nickel sites,[56] affecting as well the reduction temperature.

In the next step, all catalysts were studied by *in situ* X-ray absorption spectroscopy and *in situ* X-ray diffraction to further understand the structure of Ni and Pt species in the as-prepared samples and during reduction with H_2 (catalyst activation). In Figure 3, the XANES and the Fourier-transform (FT) k^2-weighted EXAFS spectra of the mono- and bimetallic catalysts are shown. The Ni K edge XAS spectra collected at room temperature for the monometallic Ni/$MgAlO_x$ sample (Figure 3(a)) in an inert atmosphere are depicted alongside those obtained for the metallic Ni foil, NiO, and $NiMgO_x$ references. The pre-edge feature appearing at 8333 eV for NiO $NiMgO_x$ and Ni/$MgAlO_x$ is a fingerprint of the octahedral coordination of Ni with 6 oxygen atoms. This peak derives from the 1s → 3d orbital transition, and its intensity directly correlates with the degree of geometrical distortion.[57] Noteworthy is the similarity of the XANES spectra obtained for the Ni/$MgAlO_x$ sample with that of the $NiMgO_x$ reference in terms of profile and edge step magnitude. This implies that the coordination environment and the electronic structure of Ni in the monometallic sample resemble those present in the $NiMgO_x$ reference. The differences between the white line of Ni foil, NiO, $NiMgO_x$, and the catalyst are illustrated in the inset of Figure 3(b). For Ni/$MgAlO_x$, the strong Ni−Mg interaction leading to the formation of a mixed oxide phase is additionally supported by the linear combination analysis (LCA) of the XANES data: the Ni−Mg mixed oxide represents 67% among nickel phases, while the NiO fraction is only 32%.

https://doi.org/10.1021/acscatal.3c05847
ACS Catal. 2024, 14, 7463−7477

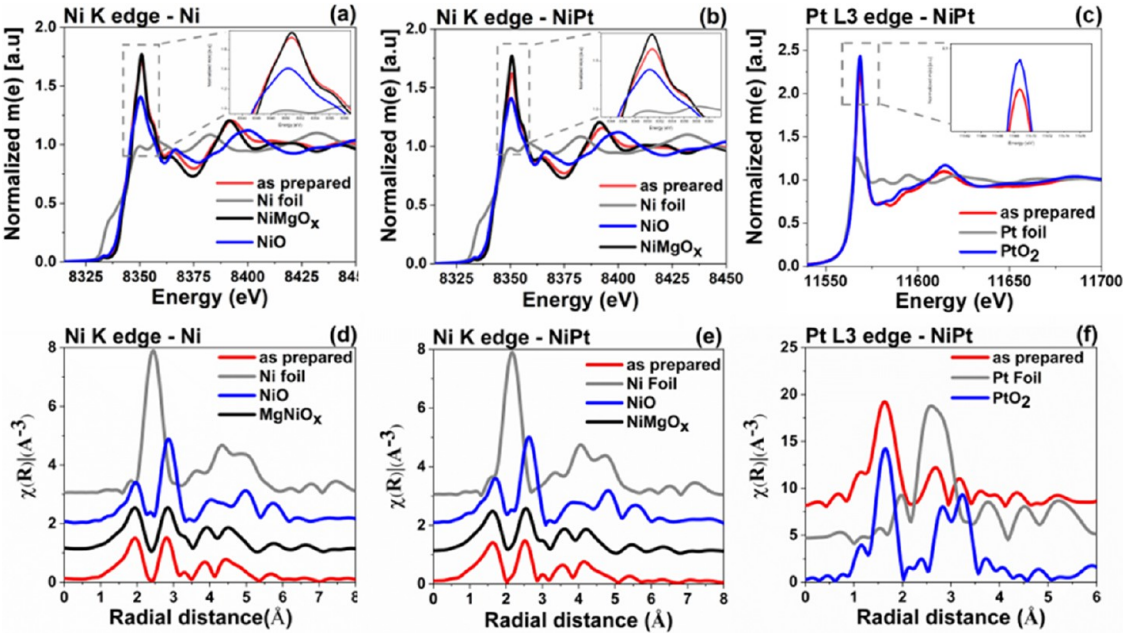

Figure 3. XANES (a–c) and FT-EXAFS (d–f) spectra recorded at Ni K and Pt L_3 edges for the as-prepared catalysts (not phase-shift corrected, k^2-weighted EXAFS). The spectra of the NiO, $NiMgO_x$, PtO_2, and Ni and Pt foil reference samples are included for comparison.

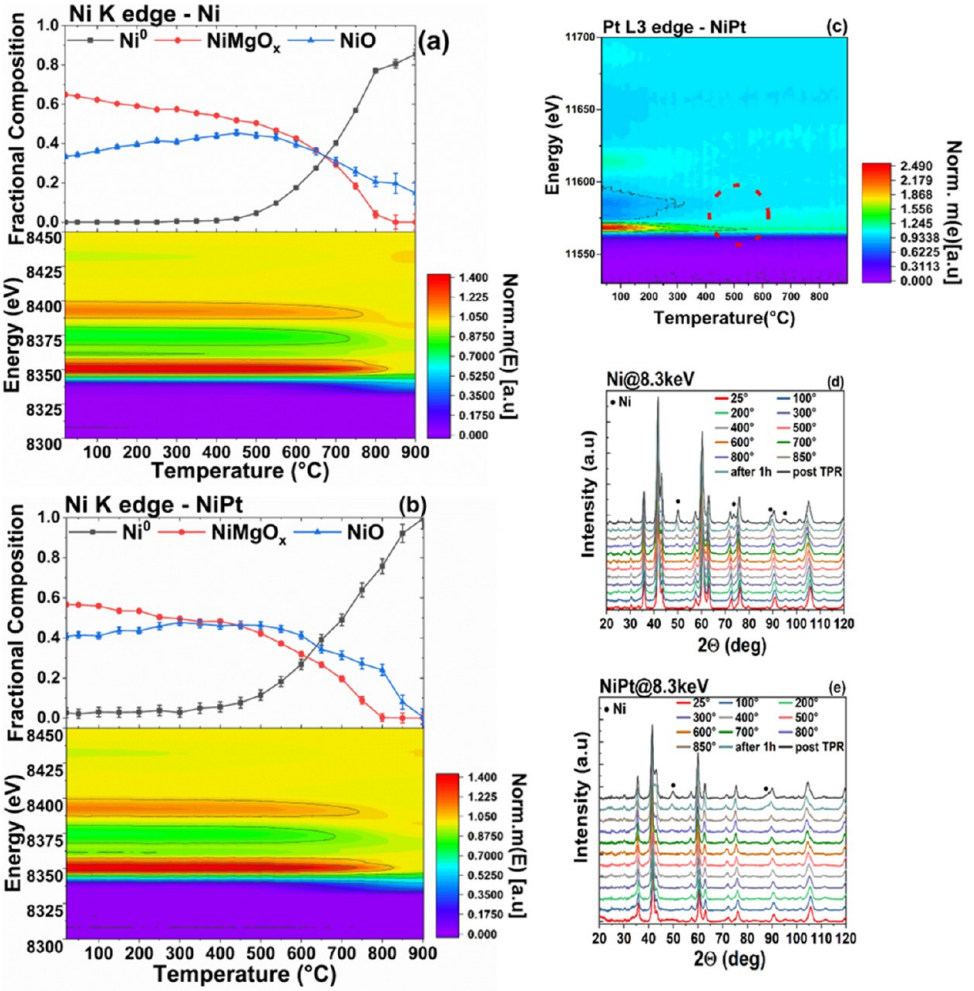

Figure 4. LCA of the *in situ* XAS spectra and the corresponding 2D-XANES map at the Ni K edge for (a) Ni/$MgAlO_x$ and (b) NiPt/$MgAlO_x$ and at the Pt L_3 edge for (c) NiPt/$MgAlO_x$ catalysts during H_2-TPR retreatment. Complementary *in situ* XRD patterns of (d) Ni/$MgAlO_x$ and (e) NiPt/$MgAlO_x$ catalysts during heating to 900 °C in 5%H_2/He at a ramp rate of 5 °C/min.

https://doi.org/10.1021/acscatal.3c05847
ACS Catal. 2024, 14, 7463−7477

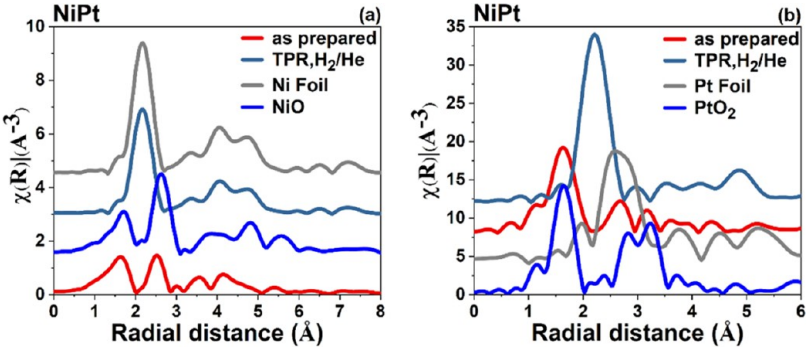

Figure 5. FT-EXAFS data recorded at (a) Ni K edge and (b) Pt L_3 edge (k^2-weighted, k = 3−12 Å^{-1}, not phase-shift corrected) of the mono- and bimetallic catalysts before and after H_2-reduction.

According to previous studies,[58,23] Ni ions substitute Mg into the MgO lattice, and the percentage of Ni in the lattice depends on the preparation method and calcination temperature. Analogous to the monometallic sample, the same features are observed in the Ni K edge XANES spectra of the bimetallic NiPt/$MgAlO_x$ catalyst (Figure 3b). The lower intensity of the edge could be explained by the slightly larger amount of NiO phase present in this sample, which, according to the LCA, is about 35%.

The local structure around the Ni atoms was additionally investigated by the analysis of the FT-EXAFS data reported in Figure 3(d,e). The results of the EXAFS data fitting (more details in Tables S1−S6 and Figures S10−S18) show that Ni is partially incorporated into the MgO lattice for both catalysts. In the as-prepared monometallic Ni/$MgAlO_x$ sample, Ni−O is the first scattering path at 2.09 Å with a coordination number of 6.2 ± 0.5, which corresponds to Ni in octahedral coordination to 6 O atoms. The second shell at 2.90 Å was found to be represented the best by a Ni−O−Mg bond in a Ni−Mg mixed oxide, in line with previous literature.[58,23] The coordination number obtained is 6.3 ± 0.4, which is lower than the value expected for the second scattering shell of a mixed oxide phase. Although the LCA analysis of the XANES region suggests the presence of NiO, no clear indication of a Ni−Ni scattering path is found at 2.95 Å in the EXAFS fitting, which could be due to the similar bond distances to those present in the Ni−Mg mixed oxide. FT-EXAFS analysis of the bimetallic NiPt/$MgAlO_x$ sample (Figure 3(e)) resulted in a similar outcome for the Ni surrounding atoms. In this case, a coordination number of 6.5 ± 0.4 was obtained for the first Ni−O scattering shell at 2.09 Å, while the Ni−O−Mg coordination sphere was found at 2.89 Å. Similarly as obtained for the monometallic Ni catalyst, the coordination number for the second coordination shell is 6.5 ± 0.6. Hence, the analysis of the XANES and EXAFS data indicates that the composition of the initial state is not so different for the mono- and bimetallic samples.

Figure 3(c) shows the XANES spectra recorded at the Pt L_3 edge for the bimetallic NiPt/$MgAlO_x$ catalyst together with those of PtO_2 and Pt foil. In the as-prepared sample, Pt was found in the oxidized state, with a comparable white line intensity as obtained for the PtO_2 reference. This suggests that Pt is well-dispersed in Ni/$MgAlO_x$. Previous studies reported the formation of Pt−O−Mg bonds, leading to an anchoring effect that prevents Pt from sintering.[59,60] However, in our study, we observed the formation of PtO_2 particles in the monometallic Pt/$MgAlO_x$ sample, which is an indicator of a rather moderate interaction with the support if temperatures up to 500 °C are applied for the catalyst preparation. With the aim of better understanding the nature of Pt−Ni and Pt−support interactions, the analysis of the FT-EXAFS spectra was also carried out for the data obtained at the Pt L_3 edge. The backscattering peak centered at 2.0 Å with a coordination number of 5.3 ± 0.5 corresponds to the first coordination shell with oxygen. The absence of further features between 2 and 3 Å suggests that there is hardly any interaction of Pt with Ni after the calcination procedure. Interestingly, there is the presence of a backscattering path at 3.0 Å, which previously was assigned to a Pt−O−Mg interaction.[60]

3.2. Activation of Ni- and Ni−Pt-based Catalysts by High-Temperature Reduction. For methane steam reforming, previous investigations showed that Ni in a reduced state is the most active species,[26] which is typically achieved by reductive treatments at high temperatures. To identify all structural changes occurring during this procedure, *in situ* XAS and *in situ* XRD measurements were conducted during catalyst reduction in 5%H_2/He. Figure 4(a) shows the LCA and the *in situ* 2D-XANES maps collected at the Ni K edge during H_2-TPR of the monometallic Ni/$MgAlO_x$ sample between room temperature and 900 °C. In the reductive atmosphere, the white line (WL) intensity of the Ni K edge, which originates from the 1s → 4p electronic transition, slowly starts to decrease above 650 °C and reaches the level of the metallic reference around 850 °C. Furthermore, the energy shift of the edge position observed at high temperatures indicates the formation of metallic Ni. The reduction temperature is well above the one expected for bulk NiO,[50] which is in accordance with our previous findings in Figure 2, and is due to $NiMgO_x$ presence in the catalyst. Based on the LCA of the XANES region, about 93% Ni^0 is present at the end of the reductive treatment (catalyst activation procedure).

For the bimetallic NiPt/$MgAlO_x$ catalyst, a similar reduction profile was observed for nickel (Figure 4(b)). The presence of Pt appears to increase the reduction rate, slightly shifting the onset reduction temperature to 300 °C. For the same catalyst, the reduction of Pt is completed at about 500 °C (Figure 4(c), starting above 150 °C). Interestingly, a shoulder appears at around 11575 eV in the Pt L_3 XANES above 400 °C. This feature (cf. reports in literature[61,62]) has been assigned to the hybridization of Ni and Pt empty orbitals in Ni−Pt alloys.[62] Overall, the impact of Pt on the reduction of the Ni species is moderate. This is probably due to the rather low concentration of the noble metal combined with the high stability of Ni-containing mixed oxides. However, at the end of the H_2-TPR

https://doi.org/10.1021/acscatal.3c05847
ACS Catal. 2024, 14, 7463−7477

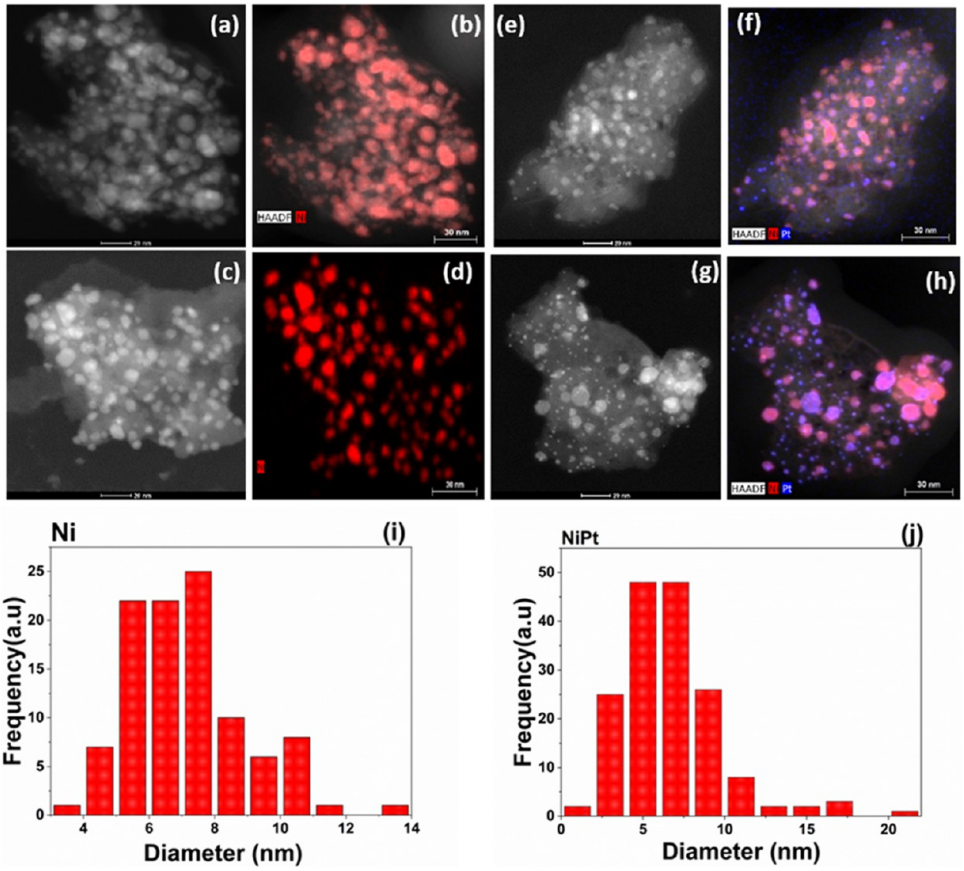

Figure 6. HAADF-STEM images with EDX mapping of Ni/$MgAlO_x$ (a–d) and NiPt/$MgAlO_x$ (e–h) samples after the H_2-TPR activation. The corresponding particle size distribution for Ni in the mono- (i) and bimetallic (l) catalysts.

procedure, i.e., 900 °C, all Ni is present in the metallic state in comparison to only 93%, as found for the monometallic sample.

Complementary *in situ* XRD patterns collected during catalyst reduction are reported in Figure 4(d,e) for the monometallic and bimetallic samples, respectively. Upon exposure to 5%H_2/He and increasing the temperature up to 850 °C, the main features appearing for both catalysts are the metallic Ni reflections at 2θ = 50° (200) and 73° (220). For both samples, they are only observed around 800 °C. After 1 h reduction, the Ni reflections at 44, 50, and 73° of the monometallic sample are sharper compared to the bimetallic counterpart. In this regard, the differences in crystallite size could be due to the strong sintering of Ni in the absence of a Pt promoter.

The detailed structure of Ni and Pt species after catalyst activation was identified by evaluating the FT-EXAFS spectra collected for the mono- and bimetallic catalysts after H_2-reduction. Visual comparison of the FT-EXAFS spectrum obtained for the reduced NiPt/$MgAlO_x$ sample with those of Ni references indicates a complete resemblance with that of metallic Ni. This assumption is further validated by the Ni–Ni coordination shell at 2.48 Å, which is identical to that of Ni in its metallic form. The fit of the first coordination shell yields a coordination number of 9.8 ± 0.3, which is low compared to that present in bulk Ni (i.e., 12). The difference could be caused not only by the size[63] but also by the flat shape of the formed metallic Ni particles,[64] which are still interacting to a certain extent with the $MgAlO_x$ support. In Figure 5(b), the FT-EXAFS spectrum recorded at the Pt L_3 edge for the as-prepared and activated NiPt catalysts is shown together with those of PtO_2 and Pt foil references. After catalyst reduction, the expected Pt–Pt backscattering of metallic Pt does not appear in the bimetallic sample. The main scattering shell located at 2.55 Å has been previously attributed to Pt–Ni in alloyed particles.[65] Hence, during the hydrogen treatment at high temperatures, Pt is not only reduced but also forming an alloy with Ni. As the alloying process is favored at moderate temperatures,[66−68] Pt will probably interact with the metallic Ni that is already available in this temperature range. The changes in the XANES profile (Figure 4(b)) indicate that the alloying process starts at 400 °C. As the temperature increases, Ni species are further reduced, which favors the increase of the Ni share in the alloy. The fitting of the FT-EXAFS data (Table S5) obtained at the end of the activation procedure indicates that Pt is in close contact with Ni, with a coordination number of 9.0 ± 0.2. The relatively high coordination number suggests that Pt is mostly inside the Ni lattice, possibly forming intermetallic $Ni_{1-x}Pt_x$ alloys or single-atom alloys.[65,69]

HAADF-STEM EDX images acquired for the activated catalysts show a broad particle size distribution for both the Ni/$MgAlO_x$ and Ni–Pt/$MgAlO_x$ samples (Figure 6). For the monometallic Ni/$MgAlO_x$ catalyst, the particle sizes range between 4 and 10 nm. Additionally, agglomerates are present on the mixed oxide support. In the bimetallic catalyst, very small Pt-rich particles (1–2 nm) are distinguished besides Ni-rich particles of sizes mostly between 2 and 10 nm (Figure 6(a–d)). This indicates a rather heterogeneous distribution of the noble metal in the bimetallic catalyst. On the one side, this could be caused by the special interactions of both Pt and Ni

https://doi.org/10.1021/acscatal.3c05847
ACS Catal. 2024, 14, 7463−7477

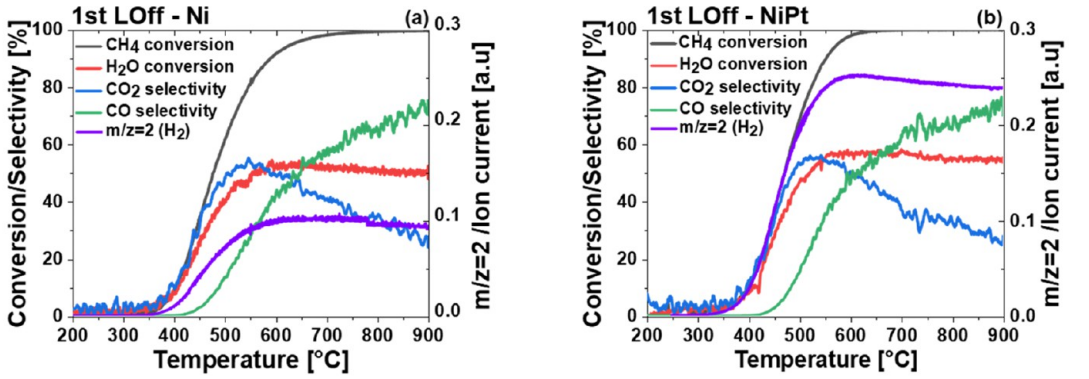

Catalyst	Ni/MgAlO$_x$			NiPt/MgAlO$_x$		
T_{50} (°C)	1^{st}	2^{nd}	3^{rd}	1^{st}	2^{nd}	3^{rd}
	510	537	544	484	497	497

Figure 7. Catalytic activity and selectivity obtained during the first MSR light-off for (a) Ni/MgAlO$_x$ and (b) NiPt/MgAlO$_x$ catalysts using a quartz capillary reactor (top); overview on the T_{50} temperatures (of 50% CH_4 conversion) measured during the heating step of the three light-off/light-out MSR cycles between 50 and 900 °C (bottom).

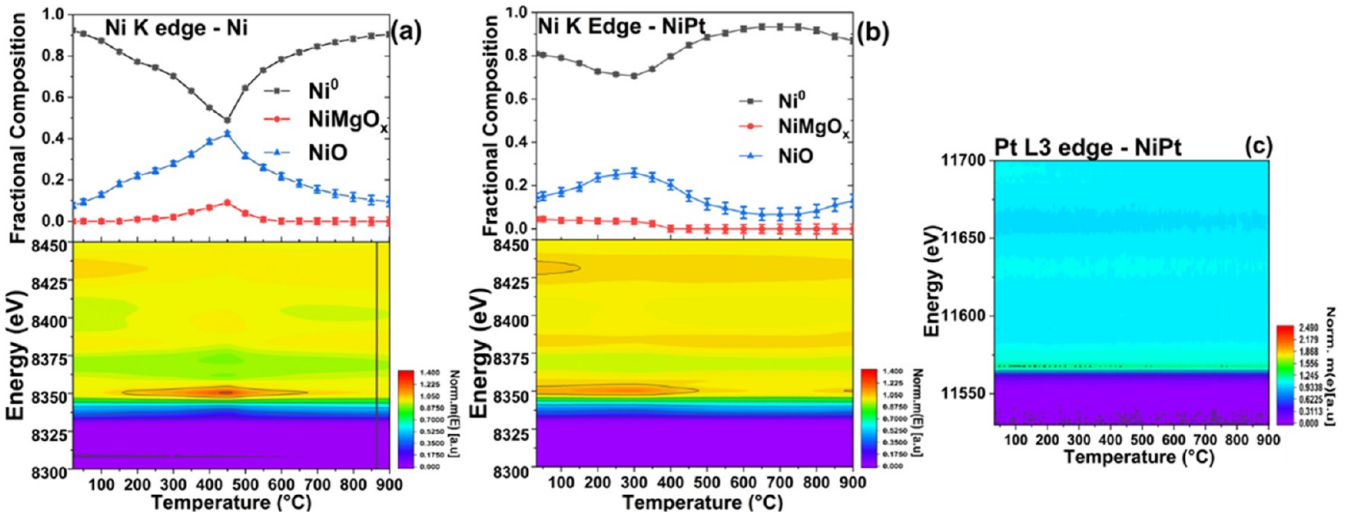

Figure 8. 2D-XANES maps and corresponding LCA of the Ni K and Pt L_3 edge XANES spectra collected during the 1st Light Off of MSR for (a) Ni/MgAlO$_x$, (b) NiPt/MgAlO$_x$ (Ni K edge), and (c) NiPt/MgAlO$_x$ (Pt L_3 edge).

with the MgAlO$_x$ support. On the other side, the different reduction temperatures of Ni and Pt species seem to favor the formation of Ni−Pt alloys with different compositions. Additionally, the rather high reduction temperature of 900 °C used for catalyst activation could lead to the sintering of Ni particles and partial segregation of Pt on the alloyed particle surface.[67] Due to the high sensitivity of the catalysts in this study to the ambient atmosphere exposure and also to the relatively high temperature required for the alloying/realloying process, the observed formation and evolution of the Pt−Ni alloyed particles could not be supplemented by other surface sensitive techniques, e.g., XPS or diffuse reflectance infrared Fourier-transform spectroscopy (DRIFTS).

3.3. Catalyst Structural Changes During Methane Steam Reforming. Methane conversion curves acquired for the monometallic Ni and bimetallic NiPt catalysts are shown in Figure 7(a,b), respectively. The catalytic performance was evaluated between 200 and 900 °C for a specific steam-to-carbon ratio (S/C) of 3, after catalyst activation in a 5%H_2/N_2 gas flow for 1 h at 900 °C. The activity and stability of the catalysts were assessed by 3 subsequent heating (L_{Off}) and cooling (L_{Out}) cycles. A about 50 °C lower onset temperature was measured for the SR reaction over the bimetallic catalyst in comparison to that recorded for the monometallic Ni/MgAlO$_x$ sample. Additionally, a progressive deactivation was noticed for the monometallic Ni catalyst, which is indicated by the higher T_{50} (temperature at 50% CH_4 conversion) measured during the second and third L_{Off}/L_{Out} cycles. In contrast, Pt addition leads to an increase in stability, in terms of the CH_4 reforming rate, throughout the three testing cycles.

In order to reveal the structural changes that cause the activity decrease for Ni/MgAlO$_x$ or the higher stability of the bimetallic sample, both Ni and Pt species were studied during *operando* XAS experiments at the Ni K and Pt L_3 edges. Figure 8 depicts the variations in the oxidation state recorded at the middle position of the catalyst bed during the first activity cycle to 900 °C for the monometallic and bimetallic catalysts (the corresponding activity is reported in Figure S1(a)). As shown

https://doi.org/10.1021/acscatal.3c05847
ACS Catal. 2024, 14, 7463−7477

in Figure 5(a,b), upon catalyst activation in a reductive atmosphere, Ni and Pt are both in a metallic state with Pt entirely alloyed with Ni. A slight oxidation of Ni species occurs immediately after exposure of the catalyst to the reaction mixture, which is more pronounced for the bimetallic catalyst (20% vs only 10% Ni^{2+} species in Ni/$MgAlO_x$) probably due to the smaller Ni particle size in this sample. Ni oxidation at low temperatures has been previously assigned to H_2O, CO_2, or traces of oxygen in specific cases.[70,71] For the monometallic catalyst, the oxidation state of Ni increases during heating in the reaction mixture from RT to 450 °C, where the fractions of metallic Ni and NiO are 48 and 42%, respectively, with the rest being present as $NiMgO_x$. Further increase in temperature results in an inversed trend in the speciation of nickel: Ni^0 becomes predominant at 900 °C and reaches 90% among all other species. The trend in the oxidation state clearly correlates with the reaction course and H_2/CO formation, which are able to reduce nickel back to the metallic state at high temperatures.

Ni species in the NiPt/$MgAlO_x$ catalyst show some mild oxidation during heating that reaches its maximum at 300 °C, just before the methane steam reforming onset. At this temperature, the extent of Ni oxidation is completely different compared to the monometallic counterpart (Ni^0 is 70%, s. above). With a further temperature increase, Ni^{2+} concentration decreases likewise as for the Ni/$MgAlO_x$ sample. At 750 °C it amounts to ∼10%, and apparently increases slightly above this temperature to 13%. The relatively broad temperature window for Ni reduction under reaction conditions despite the initial catalyst activation could indicate a possible reintercalation of Ni into the support crystal structure at lower temperatures. However, the presence of Pt in the bimetallic sample seems to attenuate the oxidation process. The shielding role of Pt toward Ni oxidation in bimetallic catalysts could be caused by the recurring diffusion of Pt toward the surface of bimetallic particles during high-temperature treatments (pre-reduction or under reaction conditions), as reported by Ahmadi et al. in a study on the behavior of PtNi nanoparticles during different annealing treatments.[72]

In contrast to the changes observed for Ni species, the profile of the Pt L_3 edge XANES spectra does not show any new features during heating to 900 °C in the reaction mixture. This indicates that Pt remains mostly in an alloyed and reduced state throughout the steam reforming process, in line with the noble character of this element (less prone to oxidation). Furthermore, this implies that Ni atoms in the close vicinity of Pt do not change their local structure and alloyed state, i.e., are not oxidized.

The sensitivity of Ni toward steam oxidation at low temperatures is visible also during cooling down from 900 to 200 °C. In the electronic Supporting Information, the linear combination analysis (LCA) for the *operando* XANES data and the corresponding catalytic activity of the mono- and bimetallic samples are provided (Figure S2). For the Ni/$MgAlO_x$ catalyst, the activity is maintained down to 500 °C when the methane concentration starts to increase. However, the oxidation state of Ni at the middle of the catalyst bed remains unchanged down to 350 °C. According to Figure S2(c), below 350 °C, the concentration of the reductive gaseous products H_2 and CO decreases, whereas the large excess of H_2O (S/C 3:1) is predominant. Consequently, Ni^0 share drops from 90% at 350 °C to 67% at 250 °C. In the same temperature range, NiO concentration increases from 9 to 21%. The difference of up to 100% is due to the appearance of $NiMgO_x$, most probably at the interface of Ni particles with the $MgAlO_x$ support.

For the bimetallic catalyst, the results shown in Figure S2(d) reveal a similar trend in Ni reoxidation at low temperatures. The final concentrations of Ni^0 and Ni^{2+} species are different: Ni^0 concentration drops from 85% at 300 °C to 72% at 200 °C, while NiO share increases from 11 to 17%. Hence, the noble metal addition contributes to catalyst stabilization by increasing the Ni reoxidation resistance. Nonetheless, owing to the low noble metal concentration, the effect of Pt on Ni is limited. Additionally, at temperatures below 500 °C and especially under oxidation conditions, the oxidation and segregation of Ni on the surface of PtNi alloys is as well expected.[73] In the next step, $NiMgO_x$ species are formed. In the bimetallic catalyst investigated here, these species amount to about 11%, which is comparable to the 12% found in the monometallic Ni/$MgAlO_x$ sample.

In line with laboratory tests (Figure 7), a decrease in activity was observed during the following activity cycles for both samples, which is clearly caused by the oxidation of Ni species. For the monometallic catalyst, a further increase of NiO and $NiMgO_x$ concentrations was noticed during the second and third L_{Offs} (Figures S3−S5). During the second L_{Off} NiO amounted to 46% and $NiMgO_x$ 23% before the methane steam reforming ignition around 600 °C. Analogous to the behavior observed during the first reaction cycle, Ni^0 concentration gradually decreases in the bimetallic NiPt/$MgAlO_x$ catalyst from 69 to 60% until 300 °C (Figure S3(d)), while Ni^{2+} increases accordingly from 20 to 30% as NiO and 10% as $NiMgO_x$. Once the reaction ignites, Ni species are reduced again to the metallic state. However, this process is slow until 900 °C for the monometallic sample, whereas for the bimetallic catalyst, the reduction achieves apparently a steady state around 600 °C during the second L_{Off}. Similar to that observed during the first cooling, Ni is partially reoxidized in both catalysts once the activity drops, amounting to a total of 44% NiO for the monometallic and 27% for the bimetallic sample. The progressive oxidation of Ni species is more pronounced for the monometallic catalyst also during the third methane steam reforming L_{Off} (Figure S5), whereas the presence of Pt maintains 50% CH_4 conversion at 450 °C, and 68% of Ni is in the metallic state for the bimetallic sample.

3.4. Catalyst Bed Structural Profiles. Overall, it could be confirmed that metallic nickel is the most active species obtained by catalyst reduction at high temperatures. However, the exposure of the catalyst to water vapors at temperatures below the methane steam reforming onset leads to partial oxidation under transient reaction conditions, a process retarded by the presence of Pt presence. Additionally, due to the strong interaction with the support, a fraction of Ni^{2+} is reincorporated into the MgO lattice. This outcome is in line with that obtained by similar studies on the catalyst state at different stages of the steam reforming process for daily startup and shutdown operation modes.[74,28,75] However, for a more precise evaluation of the extent of catalyst deactivation, which occurs for the monometallic and bimetallic NiPt catalysts, spatially resolved *operando* XAS measurements were conducted at the beginning (inlet), middle (mid), and end (outlet) positions of the catalyst bed. This approach allows us to accurately assign the drop in activity over time to the catalyst structural changes occurring in a certain zone of the reactor or in the entire catalyst bed, which, for an industrial application, corresponds to the end of the catalyst lifetime.

https://doi.org/10.1021/acscatal.3c05847
ACS Catal. 2024, 14, 7463−7477

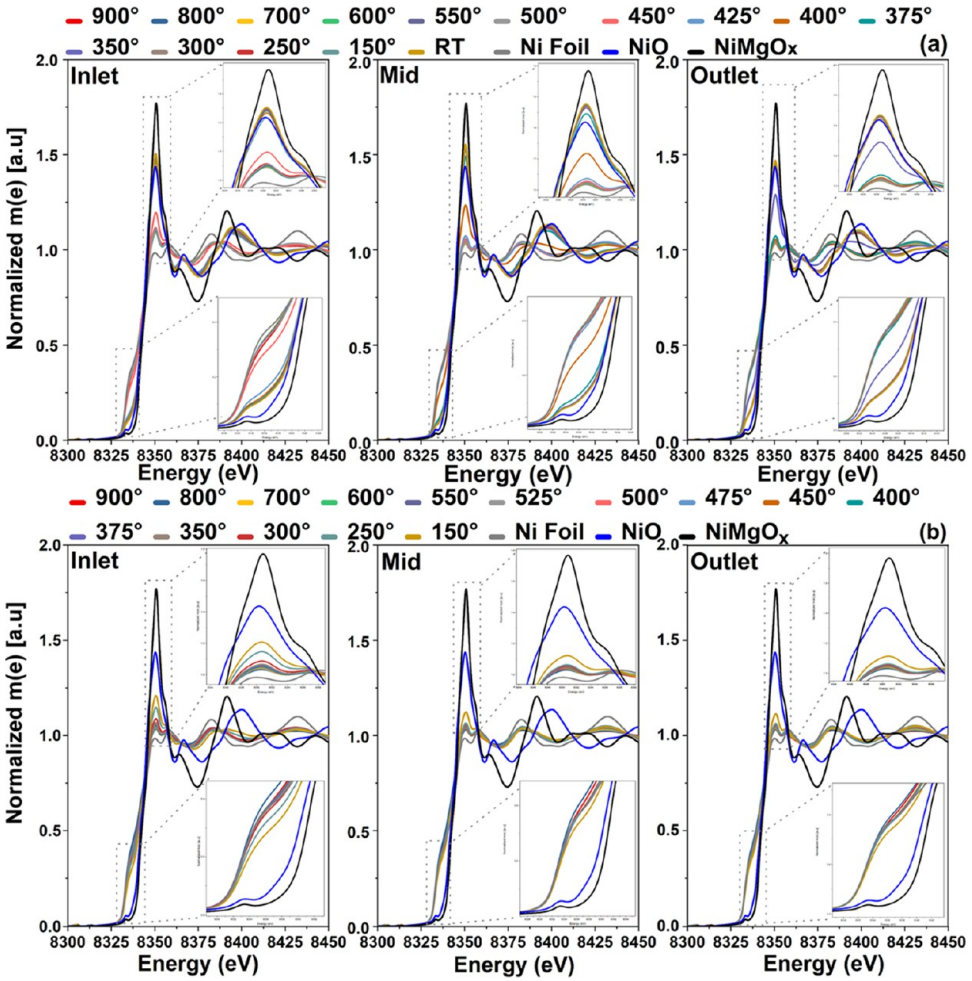

Figure 9. Spatially resolved *operando* XAS measurements at the Ni K edge at selected temperatures during the 3rd L_{Out} (cooling from 900 to 150 °C) of CH_4 steam reforming, respectively, for Ni/$MgAlO_x$ (a) and for NiPt/$MgAlO_x$ (b); inlet denotes the beginning of the catalyst bed, while outlet represents the end of the catalyst bed.

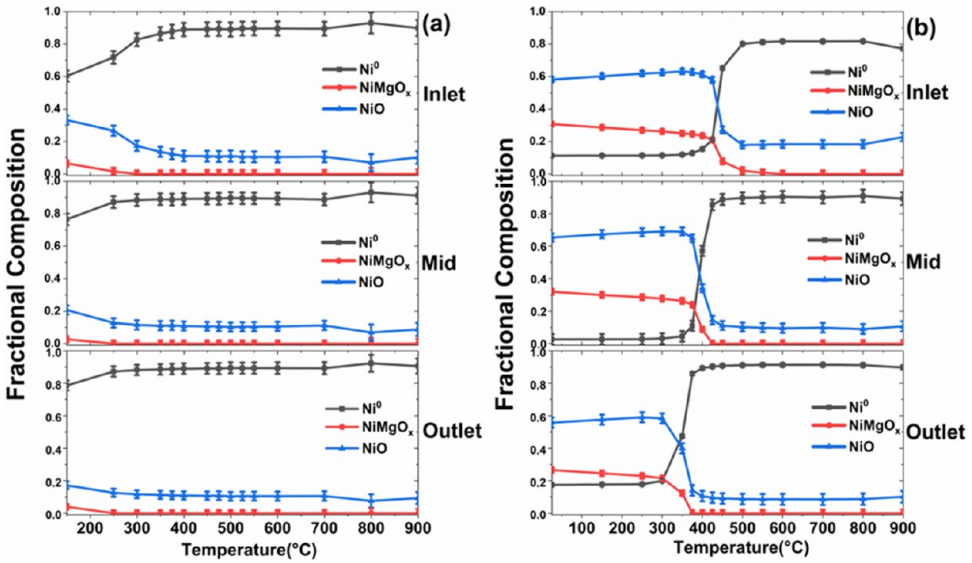

Figure 10. Linear combination analysis of Ni K edge XANES spectra acquired for (a) Ni/$MgAlO_x$ and for (b) NiPt/$MgAlO_x$ catalysts during MSR at temperatures between 900 and 50 °C (L_{Out}) for different positions of the catalys bed.

Figure 9 depicts the Ni K edge XANES spectra measured at three positions of the catalyst bed for the monometallic and bimetallic catalysts at selected temperatures during the extinction (L_{Out} of the third activity cycle) of methane SR

https://doi.org/10.1021/acscatal.3c05847
ACS Catal. 2024, 14, 7463−7477

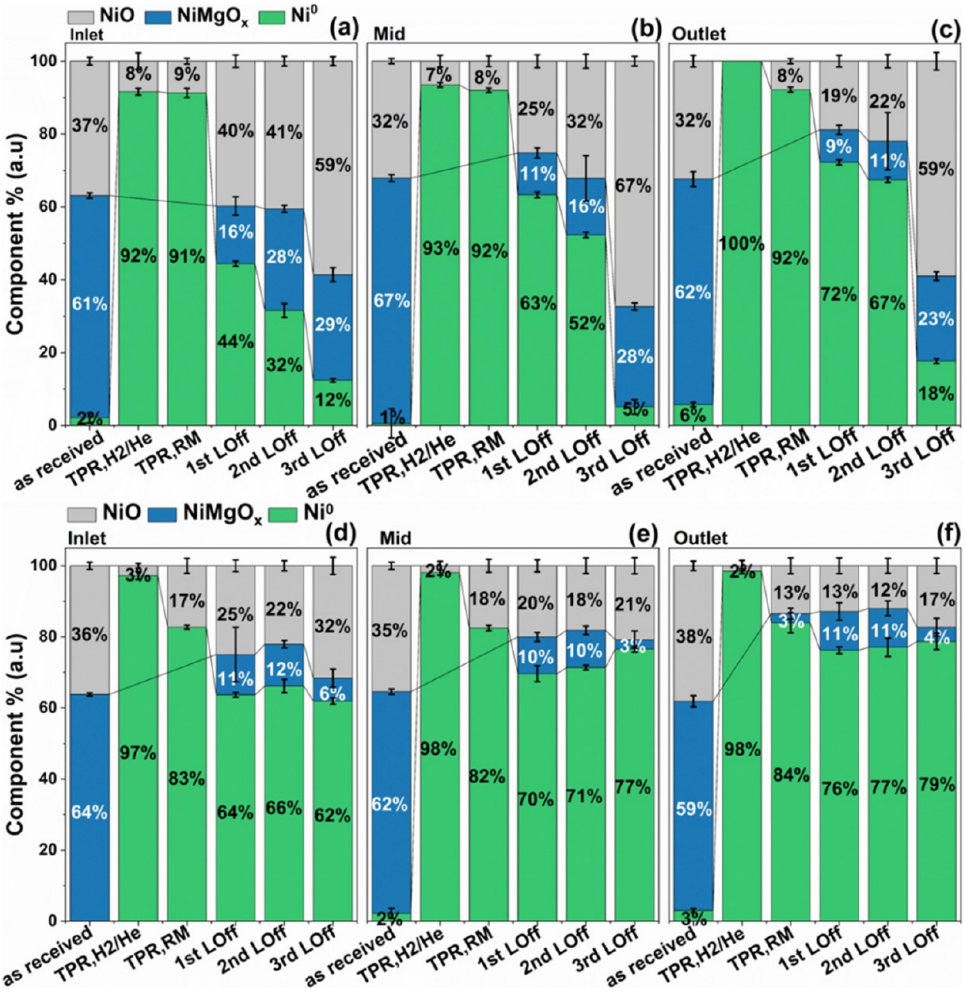

Figure 11. Linear combination analysis of the Ni K edge XANES spectra collected at room temperature at the beginning (inlet), middle, and end (outlet) positions of the catalyst bed for Ni/MgAlO$_x$ (a–c) and NiPt/MgAlO$_x$ (d–f) at different stages of the experimental procedure.

reaction between 900 and 150 °C. While Figure 9 shows the changes in the spectral features due to the temperature and gas mixture variations along the catalyst bed, the general trends in the evolution of Ni phases obtained by LCA of the XANES region are reported in Figure 10 for the inlet, middle, and outlet positions of the catalyst bed. In line with the results reported in previous sections, pronounced changes are noticed around the white line and edge position of the Ni K edge XANES spectra, as outlined in the figure insets. The increase of the white line and the shift of the edge position toward higher energy correlate with the oxidation of Ni species, resulting in NiO and NiMgO$_x$ formation. The comparison of the Ni state at the three different positions is shown in Figure 10 (results of LCA for the Ni K edge XANES region) for different reaction temperatures. For the monometallic Ni/MgAlO$_x$ catalyst (Figure 9(a,b)), more pronounced changes are noticed at the start (inlet) of the catalyst bed, with the oxidation of Ni starting around 500 °C at a CH_4 conversion of 75% (Figure S9). At 400 °C and 20% CH_4 conversion, about 90% of nickel is present as Ni^{2+} in NiO and NiMgO$_x$, an amount that remains almost unchanged during further temperature decreases. In contrast, for the bimetallic catalyst, the oxidation of Ni at the beginning of the catalyst bed is observed only around 400 °C at an overall methane conversion of 25%. In both cases, the oxidation of Ni species at this position in the catalyst bed is in line with the methane conversion profile along the reactor, progressing from the inlet toward the outlet zones. Besides the overall decrease in methane conversion during light-out (Figure S9), the inlet zone is exposed to the highest water concentration and the lowest amount of reducing gases, i.e., H_2 and CO, which generate the most favorable conditions for nickel oxidation.

Moving downstream in the catalyst bed, the oxidation of Ni species in the monometallic sample occurs only at further lower temperatures: between 450 and 300 °C and 400–250 °C at the middle and the end positions, respectively. This is due to the lower steam concentration and especially due to the more reducing gas atmosphere generated by the reaction products, i.e., H_2 (Figure S9), at these positions in the reactor. For the bimetallic NiPt/MgAlO$_x$ catalyst, a large portion of nickel remains in a reduced state even at very low methane conversion. While at the beginning of the catalyst bed, 40% of Ni is oxidized below 400 °C, and only about 20% of Ni species are in the 2+ state for the middle and outlet positions. Furthermore, at these catalyst bed positions, Ni oxidation seems to occur only below 250 °C, a process outside of the activity window for methane steam reforming. At this temperature, only about 10% of CH_4 is converted to H_2 and CO_2 (Figure S9). Despite the low amount of Pt in the bimetallic catalyst and its uneven distribution, a high

https://doi.org/10.1021/acscatal.3c05847
ACS Catal. 2024, 14, 7463–7477

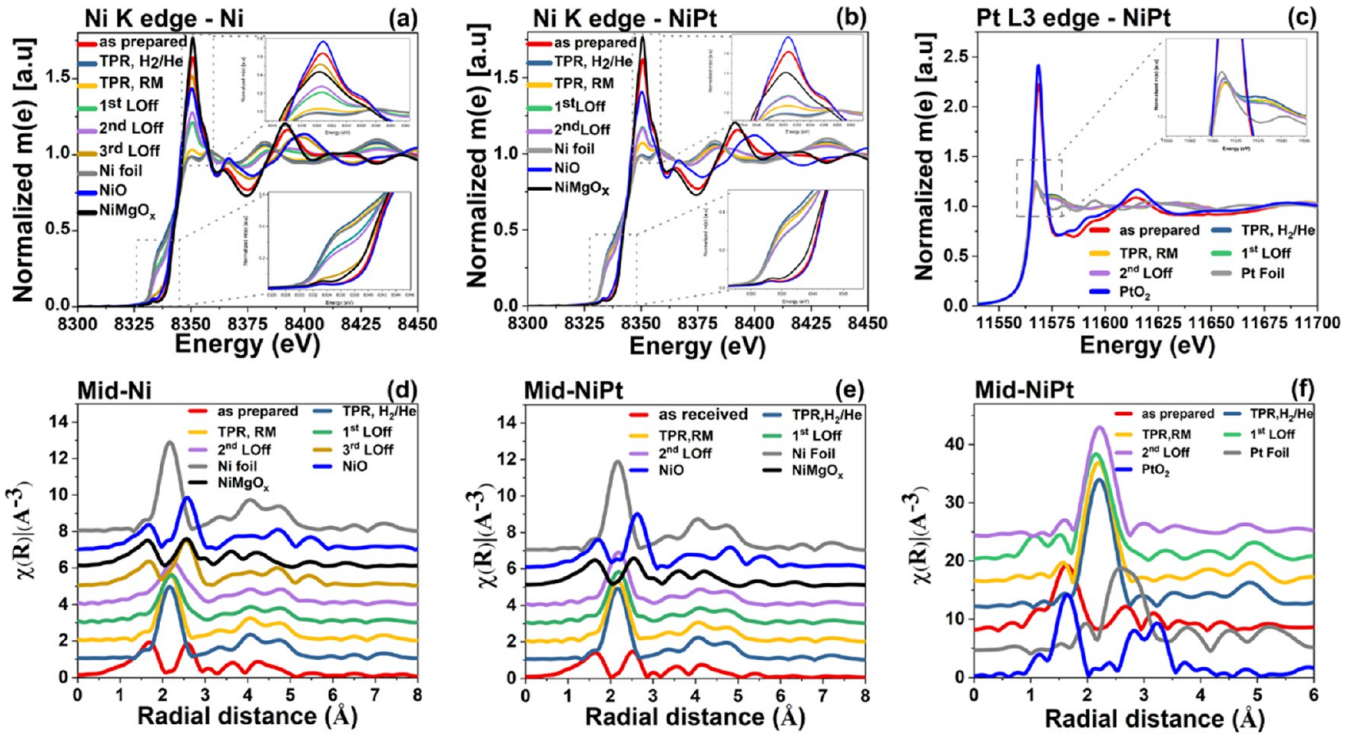

Figure 12. XANES (a–c) and FT-EXAFS (not phase-shift corrected) (d–f) spectra recorded at Ni K and Pt L_3 edges at the beginning (inlet), middle, and end (outlet) positions of the catalyst bed; the XAS spectra of NiO, $NiMgO_x$, PtO_2, Ni, and Pt foil reference samples are shown as well.

stabilization effect of the Ni metallic state is gained. The observed decrease in activity for the $NiPt/MgAlO_x$ catalyst seems rather to follow the thermodynamic equilibrium conversion, also considering the higher dissociation energy for CH_4 over Ni–Pt bimetallic surfaces versus pure Ni.[76,77] However, we cannot exclude that the decrease in activity is caused by the surface oxidation of PtNi particles at these low temperatures,[72,73] which may lead to a catalyst passivation effect.

With respect to long-term effects on catalyst structure, an overview of the evolution of Ni species in the catalyst bed from the as-prepared state upon activation and after each of the three consecutive heating/cooling cycles between room temperature and 900 °C is given in Figure 11. Ni speciation was obtained by LCA of the XANES spectra acquired at the beginning, middle, and end positions, as shown for the reduced catalyst after exposure to the reaction mixture at room temperature. As described above, by applying a calcination step to an impregnated Ni or $NiPt/MgAlO_x$ catalysts, the solid-state reaction between NiO and MgAlOx support is promoted with the formation of $NiMgO_x$ species. After reduction at 900 °C, Ni is present in the metallic state, partially alloyed with Pt in the bimetallic catalyst.

The sensitivity of Ni species toward oxidation is detected already during the initial exposure to the reaction mixture. According to the *operando* XAS results, this process is induced by the water vapors present in the gas mixture below the steam reforming onset temperature (Figure 7). Probably due to the smaller Ni-containing particles present in the NiPt sample, especially the bimetallic catalyst seems to suffer from steam oxidation under these conditions, which leads to the formation of about 18% NiO in the $NiPt/MgAlO_x$ sample. However, a progressive and more pronounced Ni oxidation is observed for the monometallic sample during the following activity cycles.

Furthermore, low reaction temperatures promote the formation of Ni–Mg mixed oxide in addition to NiO. This is confirmed by the analysis of the FT-EXAFS spectra obtained for the $Ni/MgAlO_x$ and $NiPt/MgAlO_x$ catalysts at room temperature after consecutive L_{Off}/L_{Out} cycles (Figure 12). During the stepwise cooling to room temperature, both processes start at the beginning of the reactor and rapidly evolve at downstream positions. Less than 20% metallic Ni is present at all positions of the catalyst bed at the end of the third catalytic cycle in the monometallic sample. The analysis of the corresponding FT-EXAFS data uncovers not only the formation of NiO but especially the gradual conversion of this species into the mixed oxide phase due to the solid-state reaction with MgO (Figures 12(d), S6, and S7), starting from the beginning of the catalyst bed and moving toward the outlet of the reactor. In contrast, despite its low concentration, Pt is able to drastically stabilize Ni species. Also in this case, the inlet of the catalyst bed is foremost affected as the conversion of methane is minor at this position in the reactor. However, the concentration of Ni^{2+} species shows no major variations at the three different positions during the second and third catalytic cycles for the bimetallic catalyst. This behavior is most probably related to Pt promotion of the catalyst stability.

4. CONCLUSIONS

In this study, the evolution of Ni-based mono- and bimetallic catalysts for hydrogen production by methane steam reforming was systematically analyzed under dynamic reaction conditions that are characteristic of daily startup/shutdown operation cycles. Structural changes of the oxidation state and the local structure of Ni and Pt in $15\%Ni/MgAlO_x$ and $15\%Ni\text{-}1\%Pt/MgAlO_x$ catalysts were evaluated between room temperature and 900 °C by *in situ*/*operando* XAS, whereas the overall phase composition was determined by *in situ* XRD. During the

https://doi.org/10.1021/acscatal.3c05847
ACS Catal. 2024, 14, 7463–7477

reductive activation treatment, metallic Ni particles are formed in the monometallic catalyst, while alloyed NiPt particles are generated in Ni−Pt/MgAlO$_x$. Despite most Ni particles containing Pt, a heterogeneous distribution of the noble metal was identified by HAADF-STEM investigations. *In situ* XAS measurements uncovered that this outcome is caused by the different reduction temperatures of the platinum and nickel oxides. Under reaction conditions, the oxidation of Ni species was observed. This is a pronounced and progressive process that occurs over consecutive activity cycles, in particular for the monometallic Ni/MgAlO$_x$ catalyst. Spatially resolved XAS measurements performed along the catalyst bed uncovered the start of Ni oxidation at the beginning of the catalyst bed below 500 °C, whereas the middle and end positions are only affected at lower temperatures while methane conversion decreases during cooling down of the reactor. Less than 20% of Ni is in the metallic state after 3 light-off/light-out cycles at the end of the catalyst bed, most probably present at the core of larger Ni-containing particles. Additionally, the analysis of the FT-EXAFS data uncovered the reintercalation of Ni upon oxidation into MgO lattice, leading to the formation of mixed oxide phases. Consequently, a gradual decrease in activity was observed for the monometallic catalyst during successive catalyst heating and cooling cycles in the reaction gas mixture.

Despite the relatively low loading of Pt, the noble metal presence in the bimetallic Ni−Pt/MgAlO$_x$ catalyst as alloyed Pt−Ni particles leads to a lower extent of oxidation for Ni species at low temperatures and thus too strong catalyst stabilization. According to the *operando* XAS results, the formation of Ni^{2+} as NiO and NiMgO$_x$ phases was found also in the bimetallic sample but amounting to only 20−35% of the nickel species. With only a small variation along the catalyst bed, this Ni-phase distribution was identified already after the first light-off/light-out cycle in the reaction mixture, and no further progress was recognized during the following activity tests. This behavior could be directly correlated with the activity profile obtained for this sample. In contrast to Ni evolution, Pt remains in the alloyed state with no noticeable structural changes during transient reaction conditions.

Hence, the use of *in situ*/*operando* characterization methods allowed for the first time to gain a comprehensive insight into the evolution of Ni and Ni−Pt/MgAlO$_x$ catalysts under the demanding reaction conditions of methane steam reforming. In this way, clear correlations between the Ni and Pt states and the catalyst activity could be derived over the broad temperature range of the MSR, which could serve as a fundamental basis for the rational improvement of this class of catalysts.

■ ASSOCIATED CONTENT

Supporting Information

The Supporting Information is available free of charge at https://pubs.acs.org/doi/10.1021/acscatal.3c05847.

Additional information on the catalytic activity, 2D-XANES map, and EXAFS data evaluation are reported (PDF)

■ AUTHOR INFORMATION

Corresponding Author

Jan-Dierk Grunwaldt − *Institute for Chemical Technology and Polymer Chemistry, Karlsruhe Institute of Technology (KIT), 76131 Karlsruhe, Germany; Institute of Catalysis Research and Technology, Karlsruhe Institute of Technology (KIT), 76344 Eggenstein-Leopoldshafen, Germany;* orcid.org/0000-0003-3606-0956; Email: grunwaldt@kit.edu

Authors

Enrico Tusini − *Institute for Chemical Technology and Polymer Chemistry, Karlsruhe Institute of Technology (KIT), 76131 Karlsruhe, Germany*

Maria Casapu − *Institute for Chemical Technology and Polymer Chemistry, Karlsruhe Institute of Technology (KIT), 76131 Karlsruhe, Germany;* orcid.org/0000-0002-8755-9856

Anna Zimina − *Institute for Chemical Technology and Polymer Chemistry, Karlsruhe Institute of Technology (KIT), 76131 Karlsruhe, Germany; Institute of Catalysis Research and Technology, Karlsruhe Institute of Technology (KIT), 76344 Eggenstein-Leopoldshafen, Germany;* orcid.org/0000-0002-3111-7741

Dmitry E. Doronkin − *Institute for Chemical Technology and Polymer Chemistry, Karlsruhe Institute of Technology (KIT), 76131 Karlsruhe, Germany; Institute of Catalysis Research and Technology, Karlsruhe Institute of Technology (KIT), 76344 Eggenstein-Leopoldshafen, Germany;* orcid.org/0000-0003-3930-3204

Heike Störmer − *Laboratory for Electron Microscopy, Karlsruhe Institute of Technology (KIT), 76131 Karlsruhe, Germany*

Laurent Barthe − *Synchrotron SOLEIL, 91192 Gif-sur Yvette, France*

Stephanie Belin − *Synchrotron SOLEIL, 91192 Gif-sur Yvette, France*

Complete contact information is available at: https://pubs.acs.org/10.1021/acscatal.3c05847

Author Contributions

E.T. conducted the study, performed the catalyst preparation, XAS characterization, and data analysis, and wrote the manuscript. M.C. was involved in the XAS experiments, study design, data discussion, and paper writing. D.D. and A.Z. helped with the XAS data evaluation; H.S. performed the TEM measurements; S.B. and L.B. supported the measurements at the ROCK beamline and the sample environment; J.-D.G. helped during the design of the study, discussion on the results, and paper writing. All the authors commented and gave input to the manuscript.

Notes

The authors declare no competing financial interest.

■ ACKNOWLEDGMENTS

This work was funded by the European Union's Horizon 2020 Research and Innovation program under the Marie Sklodowska-Curie Actions—Innovative Training Network (MSCA-ITN) grant agreement 813748 (BIKE Project) and the MTET program of the HGF. The work at ROCK beamline was supported by a public grant overseen by the French National Research Agency (ANR) as part of the "Investissements d'Avenir" program (reference: ANR-10-EQPX-45). Angela Deutsch is acknowledged for the help during the N_2-physisorption measurements.

REFERENCES

(1) Rostrup-Nielsen, J. R. Syngas in Perspective. *Catal. Today* **2002**, *71*, 243−247.
(2) Rostrup-Nielsen, J. 40 Years in Catalysis. *Catal. Today* **2006**, *111*, 4−11.
(3) Dincer, I. Green Methods for Hydrogen Production. *Int. J. Hydrogen Energy* **2012**, *37* (2), 1954−1971.
(4) Capurso, T.; Stefanizzi, M.; Torresi, M.; Camporeale, S. M. Perspective of the Role of Hydrogen in the 21st Century Energy Transition. *Energy Convers. Manage.* **2022**, *251*, No. 114898.
(5) Ahmed, S.; Krumpelt, M. Hydrogen from Hydrocarbon Fuels for Fuel Cells. *Int. J. Hydrogen Energy* **2001**, *26* (4), 291−301.
(6) Joensen, F.; Rostrup-Nielsen, J. R. Conversion of Hydrocarbons and Alcohols for Fuel Cells. *J. Power Sources* **2002**, *105*, 195−201.
(7) Mortensen, P. M.; Dybkjær, I. Industrial Scale Experience on Steam Reforming of CO_2-Rich Gas. *Appl. Catal., A* **2015**, *495*, 141−151.
(8) Meloni, E.; Martino, M.; Palma, V. A Short Review on Ni Based Catalysts and Related Engineering Issues for Methane Steam Reforming. *Catalysts* **2020**, *10* (3), 352.
(9) Chen, L.; Qi, Z.; Zhang, S.; Su, J.; Somorjai, G. A. Catalytic Hydrogen Production from Methane: A Review on Recent Progress and Prospect. *Catalysts* **2020**, *10* (8), 858.
(10) Yang, X. An Experimental Investigation on the Deactivation and Regeneration of a Steam Reforming Catalyst. *Renewable Energy* **2017**, *112*, 17−24.
(11) Argyle, M. D.; Bartholomew, C. H. Heterogeneous Catalyst Deactivation and Regeneration: A Review. *Catalysts* **2015**, *5* (1), 145−269.
(12) Angeli, S. D.; Monteleone, G.; Giaconia, A.; Lemonidou, A. A. State-of-the-Art Catalysts for CH4 Steam Reforming at Low Temperature. *Int. J. Hydrogen Energy* **2014**, *39* (5), 1979−1997.
(13) Kho, E. T.; Scott, J.; Amal, R. Ni/TiO_2 for Low Temperature Steam Reforming of Methane. *Chem. Eng. Sci.* **2016**, *140*, 161−170.
(14) Sehested, J. Four Challenges for Nickel Steam-Reforming Catalysts. *Catal. Today* **2006**, *111* (1−2), 103−110.
(15) Roh, H. S.; Jun, K. W.; Park, S. E. Methane-Reforming Reactions over Ni/Ce-ZrO_2/θ-Al $_2O_3$ Catalysts. *Appl. Catal., A* **2003**, *251* (2), 275−283.
(16) Purnomo, A.; Gallardo, S.; Abella, L.; Salim, C.; Hinode, H. Effect of Ceria Loading on the Carbon Formation during Low Temperature Methane Steam Reforming over a Ni/CeO_2/ZrO_2 Catalyst. *React. Kinet. Catal. Lett.* **2008**, *95* (2), 213−220.
(17) Azancot, L.; Bobadilla, L. F.; Santos, J. L.; Córdoba, J. M.; Centeno, M. A.; Odriozola, J. A. Influence of the Preparation Method in the Metal-Support Interaction and Reducibility of Ni-Mg-Al Based Catalysts for Methane Steam Reforming. *Int. J. Hydrogen Energy* **2019**, *44* (36), 19827−19840.
(18) Kumar, R.; Kumar, K.; Pant, K. K.; Choudary, N. V. Tuning the Metal-Support Interaction of Methane Tri-Reforming Catalysts for Industrial Flue Gas Utilization. *Int. J. Hydrogen Energy* **2020**, *45* (3), 1911−1929.
(19) Özdemir, H.; Öksüzömer, M. A. F.; Gürkaynak, M. A. Effect of the Calcination Temperature on Ni/$MgAl_2O_4$ Catalyst Structure and Catalytic Properties for Partial Oxidation of Methane. *Fuel* **2014**, *116*, 63−70.
(20) Sehested, J.; Gelten, J. A. P.; Helveg, S. Sintering of Nickel Catalysts: Effects of Time, Atmosphere, Temperature, Nickel-Carrier Interactions, and Dopants. *Appl. Catal., A* **2006**, *309* (2), 237−246.
(21) Bao, Z.; Zhan, Y.; Street, J.; Xu, W.; To, F.; Yu, F. Insight into the Phase Evolution of a NiMgAl Catalyst from the Reduction Stage to the Post-Reaction Stage during the Dry Reforming of Methane. *Chem. Commun.* **2017**, *53* (44), 6001−6004.
(22) Zhou, L.; Li, L.; Wei, N.; Li, J.; Basset, J. M. Effect of NiAl2O4 Formation on Ni/Al_2O_3 Stability during Dry Reforming of Methane. *ChemCatChem* **2015**, *7* (16), 2508−2516.
(23) Yoshida, T.; Tanaka, T.; Yoshida, H.; Funabiki, T.; Yoshida, S. Study on the Dispersion of Nickel Ions in the NiO-MgO System by x-Ray Absorption Fine Structure. *J. Phys. Chem. A* **1996**, *100* (6), 2302−2309.
(24) Luo, X.; Hong, Y.; Wang, F.; Hao, S.; Pang, C.; Lester, E.; Wu, T. Development of Nano NixMgyO Solid Solutions with Outstanding Anti-Carbon Deposition Capability for the Steam Reforming of Methanol. *Appl. Catal., B* **2016**, *194*, 84−97.
(25) Wang, Y. H.; Liu, H. M.; Xu, B. Q. Durable Ni/MgO Catalysts for CO_2 Reforming of Methane: Activity and Metal−Support Interaction. *J. Mol. Catal. A: Chem.* **2009**, *299* (1−2), 44−52.
(26) Saeedi, S.; Nguyen, X. T.; Bossola, F.; Evangelisti, C.; Santo, V. D. Methane Reforming Processes : Advances on Mono- and Bimetallic Ni-Based Catalysts Supported on Mg-Al Mixed Oxides. *Catalysts* **2023**, *13* (2), 379.
(27) Dal Santo, V.; Gallo, A.; Naldoni, A.; Guidotti, M.; Psaro, R. Bimetallic Heterogeneous Catalysts for Hydrogen Production. *Catal. Today* **2012**, *197* (1), 190−205.
(28) Li, D.; Nakagawa, Y.; Tomishige, K. Methane Reforming to Synthesis Gas over Ni Catalysts Modified with Noble Metals. *Appl. Catal., A* **2011**, *408* (1−2), 1−24.
(29) Grunwaldt, J. D.; Basini, L.; Clausen, B. S. *In Situ* EXAFS Study of Rh/Al_2O_3 Catalysts for Catalytic Partial Oxidation of Methane. *J. Catal.* **2001**, *200* (2), 321−329.
(30) Grunwaldt, J. D.; Beier, M.; Kimmerle, B.; Baiker, A.; Nachtegaal, M.; Griesebock, B.; Lützenkirchen-Hecht, D.; Stötzel, J.; Frahm, R. Structural Changes of Noble Metal Catalysts during Ignition and Extinction of the Partial Oxidation of Methane Studied by Advanced QEXAFS Techniques. *Phys. Chem. Chem. Phys.* **2009**, *11* (39), 8779−8789.
(31) Vogt, C.; Kranenborg, J.; Monai, M.; Weckhuysen, B. M. Structure Sensitivity in Steam and Dry Methane Reforming over Nickel: Activity and Carbon Formation. *ACS Catal.* **2020**, *10* (2), 1428−1438.
(32) Duarte, R. B.; Safonova, O. V.; Krumeich, F.; Makosch, M.; Van Bokhoven, J. A. Oxidation State of Ce in CeO_2-Promoted Rh/Al_2O_3 Catalysts during Methane Steam Reforming: H_2O Activation and Alumina Stabilization. *ACS Catal.* **2013**, *3* (9), 1956−1964.
(33) Duarte, R. B.; Nachtegaal, M.; Bueno, J. M. C.; Van Bokhoven, J. A. Understanding the Effect of Sm_2O_3 and CeO_2 Promoters on the Structure and Activity of Rh/Al_2O_3 Catalysts in Methane Steam Reforming. *J. Catal.* **2012**, *296*, 86−98.
(34) Doronkin, D. E.; Lichtenberg, H.; Grunwaldt, J. D.XAFS Techniques for Catalysts, Nanomaterials, and Surfaces. 2017, pp 75−89 .
(35) Grunwaldt, J.-D.; Caravati, M.; Hannemann, S.; Baiker, A. X-Ray Absorption Spectroscopy under Reaction Conditions: Suitability of Different Reaction Cells for Combined Catalyst Characterization and Time-Resolved Studies. *Phys. Chem. Chem. Phys.* **2004**, *6* (11), 3037−3047.
(36) Marshall, K. P.; Emerich, H.; Mcmonagle, C. J.; Fuller, C. A.; Dyadkin, V.; Chernyshov, D.; Beek, W. V.; Kvashnina, K. A New High Temperature, High Heating Rate, Low Axial Gradient Capillary Heater. *J. Synchrotron Radiat.* **2023**, *30*, 267−272.
(37) Guilera, G.; Gorges, B.; Pascarelli, S.; Vitoux, H.; Newton, M. A.; Prestipino, C.; Nagai, Y.; Hara, N. Novel High-Temperature Reactors for *in Situ* Studies of Three-Way Catalysts Using Turbo-XAS. *J. Synchrotron Radiat.* **2009**, *16* (5), 628−634.
(38) Eggart, D.; Zimina, A.; Cavusoglu, G.; Casapu, M.; Doronkin, D. E.; Lomachenko, K. A.; Grunwaldt, J. D. Versatile and High Temperature Spectroscopic Cell for *Operando* Fluorescence and Transmission X-Ray Absorption Spectroscopic Studies of Heterogeneous Catalysts. *Rev. Sci. Instrum.* **2021**, *92* (2), No. 023106. (1−9)
(39) La Fontaine, C.; Belin, S.; Barthe, L.; Roudenko, O.; Briois, V. ROCK: A Beamline Tailored for Catalysis and Energy-Related Materials from Ms Time Resolution to Mm Spatial Resolution. *Synchrotron Radiat. News* **2020**, *33* (1), 20−25.
(40) Brunauer, S.; Emmett, P. H.; Teller, E. Adsorption of Gases in Multimolecular Layers. *J. Am. Chem. Soc.* **1938**, *60* (2), 309−319.
(41) Briois, V.; La Fontaine, C.; Belin, S.; Barthe, L.; Moreno, T.; Pinty, V.; Carcy, A.; Girardot, R.; Fonda, E. ROCK: The New Quick-

https://doi.org/10.1021/acscatal.3c05847
ACS Catal. 2024, 14, 7463−7477

EXAFS Beamline at SOLEIL. *J. Phys.: Conf. Ser.* **2016**, *712*, No. 012149.
(42) Frahm, R. New Method for Time Dependent X-Ray Absorption Studies. *Rev. Sci. Instrum.* **1989**, *60* (7), 2515−2518.
(43) Frahm, R. Quick Scanning Exafs: First Experiments. *Nucl. Inst. Methods Phys. Res. A* **1988**, *270* (2−3), 578−581.
(44) Ravel, B.; Newville, M. ATHENA, ARTEMIS, HEPHAESTUS: Data Analysis for X-Ray Absorption Spectroscopy Using IFEFFIT. *J. Synchrotron Radiat.* **2005**, *12* (4), 537−541.
(45) Rostrup-Nielsen, J. R.; Sehested, J.; Nørskov, J. K. Hydrogen and Synthesis Gas by Steam- and CO_2 Reforming. *Adv. Catal.* **2002**, *47*, 65−139.
(46) Rostrup-Nielsen, J. R.Catalytic Steam Reforming. In *Catalysis: Science and Technology*; Springer Berlin Heidelberg: Berlin, Heidelberg, 1984; Vol. *5*, pp 1−117.
(47) Desjardins, K.; Mocuta, C.; Dawiec, A.; Réguer, S.; Joly, P.; Dubuisson, J. M.; Alves, F.; Noureddine, A.; Bompard, F.; Thiaudière, D. The CirPAD, a Circular 1.4 M Hybrid Pixel Detector Dedicated to X-Ray Diffraction Measurements at Synchrotron SOLEIL. *J. Synchrotron Radiat.* **2022**, *29*, 180−193.
(48) Arena, F.; Licciardello, A.; Parmaliana, A. The Role of Ni^{2+} Diffusion on the Reducibility of NiO/MgO System: A Combined TRP-XPS Study. *Catal. Lett.* **1990**, *6* (1), 139−149.
(49) Arena, F.; Frusteri, F.; Parmaliana, A.; Plyasova, L.; Shmakov, A. N. Effect of Calcination on the Structure of Ni/MgO Catalyst: An X-Ray Diffraction Study. *J. Chem. Soc., Faraday Trans.* **1996**, *92* (3), 469−471.
(50) Parmaliana, A.; Arena, F.; Frusteri, F.; Giordano, N. Temperature-Programmed Reduction Study of NiO-MgO Interactions in Magnesia-supported Ni Catalysts and NiO-MgO Physical Mixture. *J. Chem. Soc., Faraday Trans.* **1990**, *86* (14), 2663−2669.
(51) Wang, Y. H.; Liu, H. M.; Xu, B. Q. Durable Ni/MgO catalysts for CO2 reforming of methane: Activity and metal−support interaction. *J. Mol. Catal. A: Chem.* **2009**, *299* (1−2), 44−52.
(52) Luo, X.; Hong, Y.; Zhang, H.; Shi, K.; Yang, G.; Wu, T. Highly Efficient Steam Reforming of Ethanol (SRE) over CeO_x Grown on the Nano Ni_xMg_yO Matrix: H_2 Production under a High GHSV Condition. *Int. J. Energy Res.* **2019**, *43* (8), 3823−3836.
(53) Jaiswar, V. K.; Katheria, S.; Deo, G.; Kunzru, D. Effect of Pt Doping on Activity and Stability of Ni/MgAl $_2O_4$ Catalyst for Steam Reforming of Methane at Ambient and High Pressure Condition. *Int. J. Hydrogen Energy* **2017**, *42* (30), 18968−18976.
(54) Katheria, S.; Deo, G.; Kunzru, D. Rh-Ni/$MgAl_2O_4$ Catalyst for Steam Reforming of Methane: Effect of Rh Doping, Calcination Temperature and Its Application on Metal Monoliths. *Appl. Catal., A* **2019**, *570*, 308−318.
(55) Teoh, W. Y.; Doronkin, D. E.; Beh, G. K.; Dreyer, J. A. H.; Grunwaldt, J. D. Methanation of Carbon Monoxide over Promoted Flame-Synthesized Cobalt Clusters Stabilized in Zirconia Matrix. *J. Catal.* **2015**, *326*, 182−193.
(56) Foletto, E. L.; Alves, R. W.; Jahn, S. L. Preparation of Ni/Pt Catalysts Supported on Spinel ($MgAl_2O_4$) for Methane Reforming. *J. Power Sources* **2006**, *161* (1), 531−534.
(57) Yamamoto, T. Assignment of Pre-Edge Peaks in K-Edge x-Ray Absorption Spectra of 3d Transition Metal Compounds: Electric Dipole or Quadrupole? *X-ray Spectrom.: Int. J.* **2008**, *37* (6), 572−584.
(58) Izumi, Y.; Shimizu, T.; Kobayashi, T.; Aika, K. I. Nitrous Oxide Decomposition Active Site on Ni-MgO Catalysts Characterized by X-Ray Absorption Fine Structure Spectroscopy. *Chem. Commun.* **2000**, *1* (12), 1053−1054.
(59) Tanabe, T.; Nagai, Y.; Dohmae, K.; Sobukawa, H.; Shinjoh, H. Sintering and Redispersion Behavior of Pt on Pt/MgO. *J. Catal.* **2008**, *257* (1), 117−124.
(60) Okumura, K.; Hoshi, H.; Iiyoshi, H.; Takaba, H. Formation of a Pt-MgO Solid Solution: Analysis by X-Ray Absorption Fine Structure Spectroscopy. *ACS Omega* **2022**, *7* (31), 27458−27468.
(61) Moraweck, B.; Renouprez, A. J.; Hlil, E. K.; Baudoing-Savois, R. Alloying Effects on X-Ray Absorption Edges in Nickel-Platinum Single Crystals. *J. Phys. Chem. A* **1993**, *97* (17), 4288−4292.
(62) Li, L.; Zhou, L.; Ould-Chikh, S.; Anjum, D. H.; Kanoun, M. B.; Scaranto, J.; Hedhili, M. N.; Khalid, S.; Laveille, P. V.; D'Souza, L.; Clo, A.; Basset, J. M. Controlled Surface Segregation Leads to Efficient Coke-Resistant Nickel/Platinum Bimetallic Catalysts for the Dry Reforming of Methane. *ChemCatChem* **2015**, *7* (5), 819−829.
(63) Katheria, S.; Gupta, A.; Deo, G.; Kunzru, D. Effect of Calcination Temperature on Stability and Activity of Ni/MgAl2O4 Catalyst for Steam Reforming of Methane at High Pressure Condition. *Int. J. Hydrogen Energy* **2016**, *41* (32), 14123−14132.
(64) Grunwaldt, J. D.; Molenbroek, A. M.; Topsøe, N. Y.; Topsøe, H.; Clausen, B. S. *In Situ* Investigations of Structural Changes in Cu/ZnO Catalysts. *J. Catal.* **2000**, *194* (2), 452−460.
(65) Kim, S.; Sasmaz, E. Transformation of Platinum Single-Atom Catalysts to Single-Atom Alloys on Supported Nickel: TEM and XAS Spectroscopic Investigation. *ChemCatChem* **2022**, *14* (20), No. e202200568.
(66) Dahmani, C. E.; Cadeville, M. C.; Sanchez, J. M.; Morn-Lpez, J. L. Ni-Pt Phase Diagram: Experiment and Theory. *Phys. Rev. Lett.* **1985**, *55* (11), 1208−1211.
(67) Egelske, B. T.; Keels, J. M.; Monnier, J. R.; Regalbuto, J. R. An Analysis of Electroless Deposition Derived Ni-Pt Catalysts for the Dry Reforming of Methane. *J. Catal.* **2020**, *381*, 374−384.
(68) Popov, A. A.; Varygin, A. D.; Plyusnin, P. E.; Sharafutdinov, M. R.; Korenev, S. V.; Serkova, A. N.; Shubin, Y. V. X-Ray Diffraction Reinvestigation of the Ni-Pt Phase Diagram. *J. Alloys Compd.* **2022**, *891*, No. 161974.
(69) Kim, S.; Lauterbach, J.; Sasmaz, E. Yolk-Shell Pt-NiCe@SiO_2Single-Atom-Alloy Catalysts for Low-Temperature Dry Reforming of Methane. *ACS Catal.* **2021**, *11*, 8247−8260.
(70) De Coster, V.; Srinath, N. V.; Yazdani, P.; Poelman, H.; Galvita, V. V. Does CO_2 Oxidize Ni Catalysts? A Quick X-Ray Absorption Spectroscopy Answer. *J. Phys. Chem. Lett.* **2022**, *13* (34), 7947−7952.
(71) Ohi, T.; Miyata, T.; Li, D.; Shishido, T.; Kawabata, T.; Sano, T.; Takehira, K. Sustainability of Ni Loaded Mg-Al Mixed Oxide Catalyst in Daily Startup and Shutdown Operations of CH4 Steam Reforming. *Appl. Catal., A* **2006**, *308*, 194−203.
(72) Ahmadi, M.; Cui, C.; Mistry, H.; Strasser, P.; Roldan Cuenya, B. Carbon Monoxide-Induced Stability and Atomic Segregation Phenomena in Shape-Selected Octahedral PtNi Nanoparticles. *ACS Nano* **2015**, *9* (11), 10686−10694.
(73) Khalakhan, I.; Vega, L.; Vorokhta, M.; Skála, T.; Viñes, F.; Yakovlev, Y. V.; Neyman, K. M.; Matolínová, I. Irreversible Structural Dynamics on the Surface of Bimetallic PtNi Alloy Catalyst under Alternating Oxidizing and Reducing Environments. *Appl. Catal., B* **2020**, *264*, No. 118476.
(74) Li, D.; Nishida, K.; Zhan, Y.; Shishido, T.; Oumi, Y.; Sano, T.; Takehira, K. Superior Catalytic Behavior of Trace Pt-Doped Ni/Mg(Al)O in Methane Reforming under Daily Start-up and Shut-down Operation. *Appl. Catal., A* **2008**, *350* (2), 225−236.
(75) Zhan, Y.; Li, D.; Nishida, K.; Shishido, T.; Oumi, Y.; Sano, T.; Takehira, K. Preparation of "Intelligent" Pt/Ni/Mg(Al)O Catalysts Starting from Commercial Mg-Al LDHs for Daily Start-up and Shut-down Steam Reforming of Methane. *Appl. Clay Sci.* **2009**, *45* (3), 147−154.
(76) Besenbacher, F.; Chorkendorff, I.; Clausen, B. S.; Hammer, B.; Molenbroek, A. M.; Nørskov, J. K.; Stensgaard, I. Design of a Surface Alloy Catalyst for Steam Reforming. *Science* **1998**, *279* (5358), 1913−1915.
(77) Niu, J.; Ran, J.; Du, X.; Qi, W.; Zhang, P.; Yang, L. Effect of Pt Addition on Resistance to Carbon Formation of Ni Catalysts in Methane Dehydrogenation over Ni-Pt Bimetallic Surfaces: A Density Functional Theory Study. *Mol. Catal.* **2017**, *434*, 206−218.

https://doi.org/10.1021/acscatal.3c05847
ACS Catal. 2024, 14, 7463−7477